Bioactive Materials 39 (2024) 287–301

Contents lists available at ScienceDirect

Bioactive Materials

journal homepage: www.keaipublishing.com/en/journals/bioactive-materials

Advanced nerve regeneration enabled by neural conformal electronic stimulators enhancing mitochondrial transport

Hao Bai [a,1], Siqi Zhang [a,1], Huiran Yang [b], Jing Wang [a], Hongli Chen [a], Jia Li [c], Lin Li [d], Qian Yang [a], Bo Peng [e], Ziyi Zhu [b], Siyuan Ni [b], Keyin Liu [b,**], Wei Lei [a,***], Tiger H. Tao [b,f,g,h,****], Yafei Feng [a,*]

[a] Department of Orthopedics, Xijing Hospital, The Fourth Military Medical University, Xi'an, 710032, China
[b] State Key Laboratory of Transducer Technology, Shanghai Institute of Microsystem and Information Technology, Chinese Academy of Sciences, Shanghai, 200050, China
[c] Key Laboratory of Aerospace Medicine of the Ministry of Education, School of Aerospace Medicine, Fourth Military Medical University, Xi'an, China
[d] The Institute of Flexible Electronics (IFE, Future Technologies), Xiamen University, Xiamen, 361005, Fujian, China
[e] Frontiers Science Center for Flexible Electronics, Xi'an Institute of Flexible Electronics (IFE) and Xi'an Institute of Biomedical Materials & Engineering, Northwestern Polytechnical University, Xi'an, 710072, PR China
[f] Center of Materials Science and Optoelectronics Engineering, University of Chinese Academy of Sciences, Beijing, 100049, China
[g] School of Physical Science and Technology, ShanghaiTech University, Shanghai, 200031, China
[h] Institute of Brain-Intelligence Technology, Zhangjiang Laboratory, Shanghai, 200031, China

ARTICLE INFO

Keywords:
Silk materials
Electronic stimulator
Structural reconfiguration
Peripheral nerve regeneration
Mitochondrial transport

ABSTRACT

Addressing peripheral nerve defects remains a significant challenge in regenerative neurobiology. Autografts emerged as the gold-standard management, however, are hindered by limited availability and potential neuroma formation. Numerous recent studies report the potential of wireless electronic system for nerve defects repair. Unfortunately, few has met clinical needs for inadequate electrode precision, poor nerve entrapment and insufficient bioactivity of the matrix material. Herein, we present an advanced wireless electrical nerve stimulator, based on water-responsive self-curling silk membrane with excellent bioabsorbable and biocompatible properties. We constructed a unique bilayer structure with an oriented pre-stretched inner layer and a general silk membrane as outer layer. After wetting, the simultaneous contraction of inner layer and expansion of outer layer achieved controllable super-contraction from 2D flat surface to 3D structural reconfiguration. It enables shape-adaptive wrapping to cover around nerves, overcomes the technical obstacle of preparing electrodes on the inner wall of the conduit, and prevents electrode breakage caused by material expansion in water. The use of fork capacitor-like metal interface increases the contact points between the metal and the regenerating nerve, solving the challenge of inefficient and rough electrical stimulation methods in the past. Newly developed electronic stimulator is effective in restoring 10 mm rat sciatic nerve defects comparable to autologous grafts. The underlying mechanism involves that electric stimulation enhances anterograde mitochondrial transport to match energy demands. This newly introduced device thereby demonstrated the potential as a viable and efficacious alternative to autografts for enhancing peripheral nerve repair and functional recovery.

Peer review under responsibility of KeAi Communications Co., Ltd.
* Corresponding author.
** Corresponding author.
*** Corresponding author.
**** Corresponding author. State Key Laboratory of Transducer Technology, Shanghai Institute of Microsystem and Information Technology, Chinese Academy of Sciences, Shanghai, 200050, China.
E-mail addresses: keyin.liu@mail.sim.ac.cn (K. Liu), leiwei@fmmu.edu.cn (W. Lei), tiger@mail.sim.ac.cn (T.H. Tao), fengyafei2005@163.com (Y. Feng).
[1] These authors contributed equally.

https://doi.org/10.1016/j.bioactmat.2024.05.033
Received 26 February 2024; Received in revised form 4 May 2024; Accepted 17 May 2024
2452-199X/© 2024 The Authors. Publishing services by Elsevier B.V. on behalf of KeAi Communications Co. Ltd. This is an open access article under the CC BY-NC-ND license (http://creativecommons.org/licenses/by-nc-nd/4.0/).

1. Introduction

Peripheral nerve injuries (PNIs) are prevalent in the nervous system, commonly arising from trauma, disease, or surgical procedures [1]. Severe PNIs, characterized by significant nerve gaps, often result in incomplete nerve repair, potentially causing disruptions in motor, sensory, and autonomic functions [2]. Surgical intervention becomes imperative in severe PNIs [3], involving the interposition of a graft between nerve stumps as a crucial measure for substantial nerve gaps. This graft acts as a bridge, preventing excessive stretch, guiding axon growth, and supporting nerve regeneration [4]. Autografts, considered the "gold standard" for their good biocompatibility and support for Schwann and other supporting cells' extension, raise concerns about limited availability and potential neuroma formation, leading to pain and donor site morbidity [5].

Addressing these challenges requires exploring alternatives, such as artificial nerve guide conduits (NGCs) [6]. Various synthetic and natural biomaterials undergo investigation for NGCs development. Synthetic materials often pose issues like non-degradability, causing inflammatory reactions and requiring a second surgery for conduit removal [7,8]. In contrast, natural materials, known for biocompatibility and easy absorption, offer a more favorable option [9,10]. Silk, a natural material recognized for its balance of lightweight, strength, extensibility, and toughness [11], emerges as a promising biomaterial for medical endosseous devices due to its facile fabrication process, excellent biocompatibility, bioabsorbability, and plasticity [12–14]. Previous successes in producing silk bone screws and bone cement further support its viability in medical applications [15,16]. Although silk-based NGCs show promise in promoting nerve repair [3,17], their efficacy falls short of autografts due to inadequate stimuli for nerve regeneration. To overcome this limitation, our approach involves combining silk NGCs with robust and consistent stimuli to optimize current treatments and enhance the functional outcomes of repairing large-gap PNIs in humans.

Various stimuli, including physical, chemical, and biological cues, undergo investigation for their potential in promoting nerve repair [18]. Electrical stimulation, extensively studied for its impact on nerve regeneration and axon growth [19–21], demonstrates efficacy across various animal models, including sciatic, femoral, and facial nerve injuries [22–24]. Clinical evidence also supports the promotion of axon regeneration and muscle predominance through electrical stimulation [25,26]. The underlying mechanisms involve the release of neuronal brain-derived neurotrophic factor (BDNF), a signaling pathway utilizing cyclic adenosine phosphate (cAMP) as a second messenger, calcium-dependent axon regrowth, and modulation of mitochondrial function [22,27–29]. Recent work by Smith et al. suggests that electrical stimulation enhances axonal regeneration by promoting mitochondrial motility [30]. However, further experiments are necessary for a complete understanding. Delivering electrical stimulation effectively to damaged peripheral nerves without causing harm presents a significant challenge. Epidermal electrical stimulation is limited to superficial tissues [31], transcutaneous electrical stimulation carries the risk of secondary injury and infection, and has a short operating time window [32]. Self-powered devices employing piezoelectric materials can convert mechanical stimuli into electricity, enabling cost-effective and portable biomimetic conductive microenvironments [18]. Zheng et al. explored piezoelectric polymeric scaffolds, such as black phosphorus/PCL and zinc oxide-loaded PCL, for treating PNIs. Their materials repaired nerve defects and restored biomimetic microenvironments for sensory and functional activities without significant toxicity [33,34]. However, mechanical stimulation from exercise or ultrasound may risk nerve repair, and precise control of electrical signals remains a challenge for clinical applications. Wireless stimulation emerges as a potential solution, with current attempts including wireless sleeve electrodes, scaffolds based on glucose fuel cells, and inductively coupled radio stimulators [35,36]. Nevertheless, previous stimulation interfaces have been rudimentary in design, consisting of only two electrodes with low stimulation accuracy and efficiency. In order to achieve therapeutic results comparable to autologous transplantation, a more refined and efficient stimulation interface design will be required.

This study introduces a water-responsive, self-curling silk NGC incorporating a wireless electrical stimulator, denoted as SNGC-WES, with the specific aim of enhancing peripheral nerve regeneration. Self-curling solves the problem that planar electronic processes cannot fabricate complex electrodes in the inner wall of NGCs. Validation of SNGC-WES encompasses its capacity for the wireless administration of continuous and stable electrical stimulation to peripheral nerves. *In vitro* experiments substantiate the conduit's effectiveness in promoting adhesion of rat dorsal root ganglia (DRG) cells/explants and inducing axon outgrowth. Remarkably, SNGC-WES has demonstrated successful *in vivo* repair of 10 mm rat sciatic nerve defects, leading to transplanted rats exhibiting substantial improvements in both the morphology and functionality of the sciatic nerve and gastrocnemius muscle, comparable to autograft outcomes. Comprehensive molecular analyses, inclusive of mRNA sequencing (mRNA-seq), quantitative real-time polymerase chain reaction (qRT-PCR), and western blotting (WB), elucidate that SNGC-WES promotes axonal mitochondrial anterograde transport through wireless electrical stimulation transmission, thereby increasing mitochondrial density in distal axons to match energy demands. In summary, our findings underscore the considerable potential of SNGC-WES as a compelling alternative to autografts for the promotion of peripheral nerve repair.

2. Materials and methods

2.1. Fabrication of self-curling silk membrane

Bombyx mori cocoons underwent sectioning and subsequent degumming in a boiled Na_2CO_3 solution (0.02 M; Sigma-Aldrich, USA) for 30 min. The degummed cocoons were then dissolved in a LiBr solution (9.3 M; Sigma-Aldrich, USA) at 60 °C for 4 h. Following this, the resulting solution was sealed with dialysis clamps and immersed in deionized water in a beaker for 48 h at room temperature. The supernatant, denoted as the silk solution, was separated through centrifugation (18,000 r/min, 20 min, 2 times). The silk protein solution was deposited onto a rigid polymethyl methacrylate (PMMA) substrate. After 24 h of evaporation under constant temperature and humidity conditions (temperature 25 ± 2 °C, relative humidity 65 % ± 2 %), the silk membrane was carefully peeled off the PMMA substrate. This silk membrane then underwent overnight crosslinking in a vacuum drying chamber to make it insoluble in water (Fig. S1a).

The crosslinked silk membrane was completely immersed in deionized water, followed by pre-stretching and fixation under constant temperature and humidity conditions (temperature 25 ± 2 °C, relative humidity 65 % ± 2 %). The correlation between the pre-stretch length and the degree of self-shrinkage in water was examined to obtain membranes suitable for subsequent experiments. Specific pre-stretching methods were employed: 1) Water-responsive self-contractive membranes were created by pre-stretching the rectangular protein membrane in one direction and fixing it by stretching it approximately 1.5 times its original length; 2) Stable membranes were obtained by completely immobilizing the circle around the protein membrane. This resulted in the acquisition of self-contractive membranes that shrink in water and stable membranes that do not swell.

The preparation of bilayer membranes involves several meticulous steps. Initially, the surface of the uncrosslinked silk membrane is partially dissolved by wetting it with atomized water vapor. At this stage, the wetted side of the uncrosslinked film exhibits adhesive properties, crucial for the next step. Subsequently, the wetted side of the uncrosslinked membrane is carefully applied to the surface of the water-responsive self-contractive membrane, which is fixed to a rigid plate (in this study, perforated stainless steel plates were utilized). Finally, the two layers are securely fixed on the rigid plate and placed back into the

vacuum drying chamber. They are then crosslinked for 24 h, ultimately resulting in the desired bilayer membrane structure. This approach engenders a self-curling membrane, inducing curling when the inner membrane shrinks and the outer layer expands upon immersion in water or contact with body fluids. To evaluate the structural stability of the curled tube, it was immersed in a PBS solution for a duration of four weeks. Weekly inspections were conducted to accurately measure the tube diameter (Fig. S2).

2.2. Assemble of wireless electric stimulators

In this study, the design of the magnetic field receiving coil was achieved through L-EDITTM software, featuring a 1 cm diameter, 200 μm wire width, and 300 μm wire spacing. Simultaneously, the neural interface electrode, adopting a fork capacitor-like configuration with line width and spacing set at 500 μm, was also designed using the same software. The 55th Research Institute of China Electronics Technology Group Corporation executed the fabrication of photolithography masks. The preparation of the shadow mask involved using a 4-inch double-polished silicon wafer, 200 μm thick, as the base. A wet oxidation process generated a 2 μm silicon oxide layer on the wafer's surface. Subsequently, a 1.2 μm layer of MICROPOSIT S1813 photoresist was patterned on the oxide surface through photolithography, designating one side as side A and the other as side B. Patterns were achieved through the Reactive Ion Etching (RIE) process. Using the patterned silicon oxide as the mask, a deep silicon etching process was employed, reaching an etching depth of approximately 200 μm on side B. Finally, the silicon oxide layer on both sides was removed using buffered oxide etch (BOE), completing the fabrication of the shadow mask for silk protein device patterning (Fig. S1b).

The fabrication of the silk device involved affixing various types of membranes to new wafers. The shadow mask was meticulously attached to the membrane surface and secured with high-temperature tape. A metallic pattern (Metal: Titanium (Ti)/Aurum (Au); Thickness: 100/1500 A) was deposited onto the silk membrane using an electron-beam evaporation process. The stimulation interface was applied to the self-curling silk membrane, while inductive coils were plated onto the stable silk membrane (Fig. S1b). These components (inductor coils, stimulus interfaces) were assembled through a thermal pressure welding process using anisotropic conductive film (ACF) at 130 °C and 0.6 MPa. Previous reports of our project team have confirmed that electrodes fabricated according to the aforementioned method are capable of maintaining consistent and stable functionality *in vivo* [37,38].

2.3. Evaluation of material morphology and mechanical properties

The microstructure and surface of SNGC-WES underwent examination using a scanning electron microscope (SEM; S–3400 N, Hitachi, Japan) operating at an accelerating voltage of 5 kV. Mechanical properties of the conduits were evaluated with a tensile-testing machine (M1600, Schenk AG, Germany). Membranes, each measuring 5 cm in length, were clamped with a 3 cm inter-clamp distance and pulled longitudinally at a rate of 1 mm/s until rupture. The Young's modulus and fracture stress were determined using the following formulas: Young's modulus = σ/ε, where σ represents stress and ε denotes strain, and Fracture stress = F/S, with F representing the maximum force upon material rupture and S being the cross-sectional area of the material.

Considering that silk biodegradation is primarily enzymatic and slow *in vivo*, this study focused on *in vitro* examination of biodegradation using proteinase K (Biofroxx, Germany) to investigate the biodegradation properties of SNGC-WES. After immersing SNGC-WES in a 0.1 mg/mL proteinase K solution, the equipment was dried and weighed daily to monitor the rate of weight loss. Weight loss was calculated using the formula: Weight loss = $(W_0–W)/W_0$, where W_0 represents the initial weight of the material, and W is the real-time weight of the material.

2.4. Electrical measurements

Resistance Detection: After assessing the initial resistance (R_0), the SNGC-WES was immersed in deionized water for one month, and real-time resistance (R) was monitored at 24 h intervals. The ratio R/R_0 was utilized to characterize the extent of change in stimulator resistance. Electrical Stimulation Transmission Efficiency: The strength of the induced electromotive force depends on the rate of change of magnetic flux in the receiving coil. A dual-coil configuration was used as a transmitting antenna to generate the magnetic field. A custom-made stand was leveraged to ensure consistency in the positional relationship between the two coils. In addition, these coils were aligned parallel to each other, referencing the center, and maintained a consistent 10 mm spacing. Employing a functional signal generator, an electrical signal (1–20 V, 20 Hz, bi-directional square wave) was input into the transmitting antenna. Subsequently, the magnetic field transmitting coil was coupled to the receiving coil of the SNGC-WES (coil distance 10 mm). The electrical signals emitted from the SNGC-WES were captured by an oscilloscope (RIGOL, China).

2.5. Cytotoxicity tests

The silk membrane underwent sterilization by cutting it into 1 × 1 cm squares and exposing it to cobalt radiation (Co 60, 10–130 Gy/min, The Fourth Military Medical University, China). PC12 cells (PriMed-iCell-026, Sabakon, China) were cultured on the membrane in 1640 medium supplemented with 10 % fetal bovine serum (FBS; Gibco, USA). After a 48-h incubation period, the original medium was replaced with Live/Dead staining solution (Solarbio, China), and the incubation continued for an additional hour. Fluorescent staining was then observed using a confocal microscope (LSM 510 META; ZEISS, Germany). Cell proliferation, as per ISO 10993-12 guidelines, was assessed by soaking silk membranes in 1640 medium supplemented with 10 % FBS (6 cm^2/mL) at 37 °C for 24 h to obtain extracts. PC12 cells were seeded into 96-well plates and cultured in the extracts for 3 days, with cells cultured in 1640 medium (Hyclone, USA) supplemented with 10 % FBS serving as controls. Cell proliferation was determined at 24, 48, and 72 h using the cell counting kit-8 (CCK-8, Biosharp, China). Briefly, the medium was aspirated from each well, and 100 μL of medium mixed with 10 % CCK-8 was added. After incubating for 1 h at 37 °C in a 5 % CO_2 incubator (Thermo Fisher, USA), absorbance was measured at 450 nm using enzyme labeling equipment (FLUOstar Omega; BMG Labtech, Germany).

2.6. In vitro axon outgrowth and immunofluorescence analysis

Isolation of DRG explants and cells from postnatal day 3 Sprague Dawley (SD) rat pups followed a previously described procedure [39]. Briefly, the neonatal rat's head was severed, and the spinal canal was incised along the midline to expose the DRG. Extracted dorsal root ganglias were dissected and digested in a solution composed of 50 % trypsin (Solarbio, China) and 50 % collagenase type IV (Gibco, USA). Digestion durations were 5 min for DRG explants and 1 h for DRG cells. Post-digestion, DRG explants/cells were cultured in nerve maintenance solution, including 50 mL neurobasal medium (Thermo Fisher, USA), 1 mL B27 (Thermo Fisher, USA), 500 μL glutamine (Beyotime, China), 500 μL Penicillin-Streptomycin (Invitrogen, UK), and 25 μL nerve growth factor (Peprotech, USA). To evaluate explants/cells adhesion and axon outgrowth, we cultured DRG explants/cells in confocal dishes, the inner layer of silk NGC, and the inner layer of SNGC-WES. Electrical stimulation (200 mV/mm, 20 Hz, pulse, 5 d, 1 h/d) was administered to the SNGC-WES group explants after 24 h of culture. Immunofluorescence staining of DRG cells and explants was conducted post-electrical stimulation. Briefly, cells were fixed in 4 % paraformaldehyde (Beyotime, China) and incubated overnight at 4 °C with a primary antibody (1:400, Proteintech, China). Subsequently, they were incubated with a

secondary antibody (1:400, Proteintech, China) at room temperature for 1 h before being observed under a confocal microscope. Fluorescent images of explants/cells were analyzed using ImageJ software. Sholl analysis assessed neurite length by generating circles of defined growing radii based on a virtual midpoint, counting intersections of the circles with neurites. Only the first occurrence of an intersection was considered to avoid overlapping neurite counts. The distance between adjacent radii was 50 μm. Neurite outgrowth was also evaluated based on the average length of the 15 longest axons.

2.7. Surgical procedure

Exploration of *in-vivo* therapeutic effects involved a critical nerve gap model employing the sciatic nerve in rodents. Adherence to institutional guidelines of the Chinese PLA Air Force Military Medical University was paramount in all animal-related procedures. The experimental protocol was reviewed and approved by the institutional animal care and use committee at the Chinese PLA Air Force Military Medical University. Adult male SD rats (Charles River Laboratories), weighing 200–250 g, were used in the following experiments with each group comprising 5 animals. Four distinct experimental groups were delineated: 1) untreated defects (Control group); 2) repair with autologous nerve grafts (Autograft group); 3) application of a simple silk conduit (Conduit group); 4) SNGC-WES with electrical stimulation (SNGC-WES group). The left hind limb was shaved and sterilized with iodophor. A 1.5 cm incision was made on the skin, revealing the sciatic nerve, from which a 10 mm nerve segment was excised. In the Conduit and SNGC-WES groups, the proximal and distal ends of the severed sciatic nerve were seamlessly sutured using a nerve epithelial suture technique, employing 9-0 nylon surgical sutures, with precision at the 1 mm margin of the corresponding conduit ends. The inductive element for wireless stimulation was implanted into adjacent subcutaneous layers. In the Autograft group, the severed 10 mm nerve segment was repositioned and re-sutured with the nerve stumps. For the control group, the nerve segment was resected without any intervention.

2.8. Protocol for proximal nerve stimulation

The application of instantaneous wireless stimulation, facilitated by a waveform generator (UNI-T, China), involved the utilization of variable magnetic flux. Implanted stimulators were activated wirelessly to administer electrical stimulation (biphasic, square waveform, 200 μs pulse width, 20 Hz frequency, minimum amplitude over threshold, 1.6 V) to the injured nerve for 1 h/day. Rats in the SNGC-WES group were subjected to uninterrupted electrical stimulation for 14 days.

2.9. Gait function analysis

Assessment of functional muscle reinnervation involved the use of the sciatic nerve function index (SFI) and static sciatic index (SSI). Hindfoot footprints and morphology of rats were collected (Fig. S3a). Paw print parameters, including print length on both sides (EPL, NPL), toe spread (distance from toe 1 to toe 5) on both sides (ETS, NTS), and the distance from toe 2 to toe 4 on both sides (EIT, NIT), were measured (Fig. S3b). The computation of SFI and SSI employed the following formulas: $SFI = 38.3\ [(EPL-NPL)/NPL] + 109.5\ [(ETS-NTS)/NTS] + 13.3\ [(EIT-NIT)/NIT]$; $SSI = [108.44 \times (ETS - NTS)\ NTS + 31.85 \times (EIT - NIT)/NIT] - 5.49$. Values approaching 0 for SFI and SSI indicated enhanced recovery, while values close to −100 indicated complete impairment.

2.10. Electrophysiology measurements

Electrophysiological evaluations were conducted at 4-, 8-, and 12-weeks post-surgery. Under anesthesia, the sciatic nerve on the operated side was re-exposed, and electrical stimulation was applied to the proximal and distal ends of the nerve graft. The compound muscle action potential (CMAP) was recorded on the gastrocnemius muscle belly (Fig. S3c). CMAP latency, indicating the time from stimulus onset to the initial deviation of the CMAP curve from baseline, was measured. The nerve conduction velocity (NCV) was calculated using the formula: $NCV = (t_1 - t_2)/d$, where t_1 is the time of proximal electrical stimulation, t_2 is the time of distal electrical stimulation, and d is the distance between the two stimulation sites (Fig. S3d). The pulse mode was configured with a frequency of 1 Hz, duration of 1 ms, and a magnitude of 39.2 mA.

2.11. Histological analyses on regenerated nerves

The regenerated sciatic nerves, obtained 12 weeks post-surgery, underwent thorough examination. For nerve fiber analysis, the harvested nerves were immobilized and sectioned into 8 μm slices. The nerve morphology was examined through fluorescent staining. The visualization of regenerated axons was achieved using a rabbit anti-β3-tubulin antibody (diluted 1:400; R&D Systems, Inc., USA), while Schwann cells were visualized using a rabbit anti-S100 antibody (diluted 1:400; R&D Systems, Inc., USA). Cy3-labeled goat anti-rabbit antibody (1:200; Abcam, UK) served as the secondary antibody, and DAPI (Sigma-Aldrich, USA) was applied for staining the cell nuclei. The samples were observed and photographed using a confocal microscope (LSM 510 META; ZEISS, Germany). For the myelination analysis of regenerated nerve fibers, the nerve was washed with normal saline, fixed with 2.5 % glutaraldehyde (Invitrogen, USA) at 4 °C for 24 h with autografts and conduits peeled and sliced into 50 nm sections for observation under a transmission electron microscope (TEM) (HT7700, Hitachi, Japan). ImageJ software was utilized for the detailed analysis of TEM images, including the calculation of g-ratio (Fig. S3e), axon diameter and myelin sheath thickness.

2.12. Histological analyses on gastrocnemius muscle

Upon reaching the 12-week post-surgery, both sides of the gastrocnemius muscles were extracted and weighed, with the recorded values represented as a ratio (left/right). Specimens were procured from the mid-belly region of the gastrocnemius muscle, fixed in 4 % paraformaldehyde (Beyotime, China), and then embedded in paraffin wax. Transverse sections, each with a thickness of 10 μm, were cut and subjected to hematoxylin and eosin (HE) and van Gieson (VG) staining. Five cross-sectional fields containing muscle fibers were randomly chosen and analyzed using ImageJ. The percentage of muscle fiber area was calculated based on the proportion of the muscle fiber area to the total field area.

2.13. Transcriptome sequencing (mRNA-seq) and analysis

Extraction and evaluation of total RNA from both unstimulated and electrically stimulated DRG cells were performed using an Agilent 2100 Bioanalyzer (Agilent Technologies, Palo Alto, CA, USA), with further validation conducted through RNase-free agarose gel electrophoresis. Eukaryotic mRNA enrichment was achieved via Oligo(dT) beads after total RNA extraction, followed by transcription of the enriched mRNA into cDNA. The resulting library underwent sequencing using Illumina Novaseq6000, conducted by Gene Denovo Biotechnology Co. (Guangzhou, China). DESeq2 software was used for analysis of differential expression in RNAs between the two distinct groups. Genes/transcripts with a false discovery rate (FDR) parameter below 0.05 and an absolute fold change of ≥ 2 were identified as differentially expressed genes (DEGs)/transcripts. Finally, Kyoto Encyclopedia of Genes and Genomes (KEGG) pathway and Gene Ontology (GO) enrichment analyses were executed using the DAVID database.

2.14. Quantitative real-time polymerase chain reaction (qRT-PCR)

Total cellular mRNA from both unstimulated and electrically stimulated DRG cells was extracted using Trizol reagent (Thermal Fisher, USA). Subsequently, 1 μg of mRNA in each group underwent reverse transcription to cDNA. qRT-PCR was performed using SYBR Premix Ex Taq (TaKaRa, Japan) to detect specific mRNA transcripts following the manufacturer's instructions. Thermal reaction conditions for quantitative PCR were set as follows: 95 °C for 30 s; followed by 40 cycles of 95 °C for 5 s and 60 °C for 30 s; followed by 95 °C for 15 s, 60 °C for 1 min, and 95 °C for 15 s. Relative mRNA levels were calculated utilizing the $2-\Delta\Delta Ct$ method. Reverse primers were listed in Table S1.

2.15. Western blotting

Protein expression was evaluated through WB analysis. After induction with NGF for 24 h, DRG cells, both unstimulated and electrically stimulated were lysed in RIPA buffer (Beyotime, China) containing 1 × protease inhibitor cocktail (Thermo Fisher, USA). Protein concentrations were determined using the BCA Protein Assay (Beyotime, China). Equal protein amounts were loaded in triplicate for each group and separated through 10 % SDS-PAGE gels. Subsequently, the proteins were transferred to a PVDF membrane, followed by blocking with 5 % nonfat milk in Tris Buffered Saline with Tween (TBST) at room temperature for 2 h. Primary antibodies (1:1000, Abcam, UK) were incubated overnight at 4 °C, and secondary antibodies (1:5000, Proteintech, China) were applied at room temperature for 1 h. The anticipated bands were visualized using enhanced chemiluminescence detection reagents.

2.16. Intracellular Ca^{2+} fluorescence imaging and quantification

Intracellular Ca^{2+} concentrations were assessed utilizing the calcium indicator Fluo-4, AM (Yeasen, China). Following washing with Phosphate Buffered Saline (PBS), DRG cells—both unstimulated and electrically stimulated—were treated with Fluo-4, AM working solution, ensuring comprehensive coverage. The cells were then incubated at 37 °C for 60 min, and then the Fluo-4, AM working solution was removed. After a further washing step, an additional 30-min incubation at 37 °C was performed to ensure complete de-esterification of AM groups within the cells. The observation of cells was carried out using a confocal microscope.

To quantify the intracellular Ca^{2+} concentration following electrical stimulation, flow cytometric techniques were employed in PC12 cells. In brief, electrical stimulation (200 mV/mm, 20 Hz, pulse, 5 d, 1 h/d) was administered to the SNGC-WES group cells after 24 h of culture. Calcium fluorescent probes (Fluo-4, AM, 4 μmol/L) were then loaded on stimulated and non-stimulated cells. Cells were incubated in an incubator for 60 min before being washed and resuspended by calcium-free buffer. Fluorescence intensity measurements of individual cells in the cell suspension samples were conducted using flow cytometry.

2.17. Time-lapse imaging and kymograph analysis

For labelling mitochondria, DRG explants were subjected to a 4-h incubation with MitoTracker staining solution (Thermo Fisher, USA). Time-lapse imaging of the microgrooves was recorded using a confocal microscope (LSM 510 META; ZEISS, Germany) equipped with a C-Apochromat 40 × /1.3 oil NA objective (ZEISS). Image sequences were captured at a resolution of 512 × 512 pixels (12 bit), maintaining 5-s intervals and a scanning zoom of 1.0 in the x and y directions; 60 frames were acquired for each condition. To quantify motility, a kymograph was generated, classifying mitochondria as stationary if their trajectories remained perpendicular throughout the recording period and in motion if otherwise.

2.18. Statistical analysis

Statistical analyses were conducted with GraphPad Prism (version 6.0), employing a *t*-test and one-way analysis of variance (ANOVA). Significance was denoted by $P < 0.05$ and represented as *, #, and $. Unless explicitly stated otherwise, the reported results are expressed as mean ± SD. Image analysis was performed using ImageJ (NIH, USA).

3. Results and discussion

3.1. Physical and chemical characterization of SNGC-WES

We created water-responsive self-curling silk membranes and stable silk membranes using fibroin extracted from *Bombyx mori* silkworm cocoons, as depicted in Fig. 1a and b. The wireless stimulator components were then integrated onto the surfaces of both self-curling and stabilized membranes. Silk's exceptional properties, distinct from many other biomaterials [40], posed a challenge due to its water-induced swelling, affecting the maintenance of a metallic circuit structure on its surface. To address this issue, we subjected silk membranes to directional pre-stretching and stabilized drying post qualitative crystalline orientation. These membranes underwent molecular conformation changes upon water exposure, resulting in either stabilization or retraction based on the degree of stretching (Fig. 1a). Furthermore, we introduced a water-responsive self-curling silk membrane (Fig. 1b), deviating from Yi et al.'s water-responsive soft film concept [41], as our process transforms the material's 2D structure into a 3D structure. This innovative approach not only protects metal circuits during membrane curling but also facilitates cell loading to enhance nerve repair. It can envelop incompletely severed or sutured nerves, broadening its applications. The assembly of SNGC-WES involved ACF welding and cross-linking of membranes for each component (Fig. 1c). Fig. 1d illustrates the stimulator, emphasizing the magnetic field harvester, signaling circuit, and electrical interface to the targeted peripheral nerve. The magnetic field harvester detects changes in magnetic flux subcutaneously, generating an induced electromotive force. Simultaneously, the electrical interface, in direct contact with nerve stumps, was designed for stimulation, featuring exposed Au electrodes encircling the nerve and a self-curling silk membrane curled into a tube.

Post-fabrication, the electrical interface demonstrated excellent self-curling performance after a 10-min water immersion (Fig. 2a). SEM images validated the robust continuity and tight welding of the bilayer structure (Fig. 2a). With a hole diameter of 1 mm and an average wall thickness of 100 μm, the SNGC-WES equipped a magnetic field harvester configured as a loop antenna in a bilayer, dual-coil setup (~50 μm thick), integrating an Au circuit (15 μm thick, 200 μm wide). The Au circuit, arranged in a serpentine geometry with an opening at the end, served as an electrical extension and connection for delivering electrical stimulation to nerve tissue. The relationship between the degree of pre-stretching of silk membranes and self-contraction upon water contact is depicted in Fig. 2b. Mechanical testing revealed the Young's modulus and fracture stress of the stable membrane as 7.4 MPa and 6.0 MPa, respectively, and for the self-curling membrane as 22.8 MPa and 7.6 MPa, respectively (Fig. 2c and d). These results demonstrated the suitability of the membranes' mechanical properties for nerve conduits [3].

Peripheral nerve regeneration via electrical stimulation is predominantly influenced by stimulation intensity, stability, and duration [20]. Fig. 2e–g provide a summary of the electrical performance characteristics of the wireless electrical simulator. The change in magnetic flux depends on the current alteration in the transmitting antenna. When the transmission antenna received a sustained square-wave electrical transmission (10 V, 20 Hz over a 10 mm coupling distance), the harvester generated a biphasic pulse output of 0.6 V, 20 Hz (Fig. 2e). As shown in Fig. 2f, a significant linear relationship exists between transmitted voltage and output voltage at a distance of 10 mm. Additionally, the stimulator's resistance exhibited no significant change within

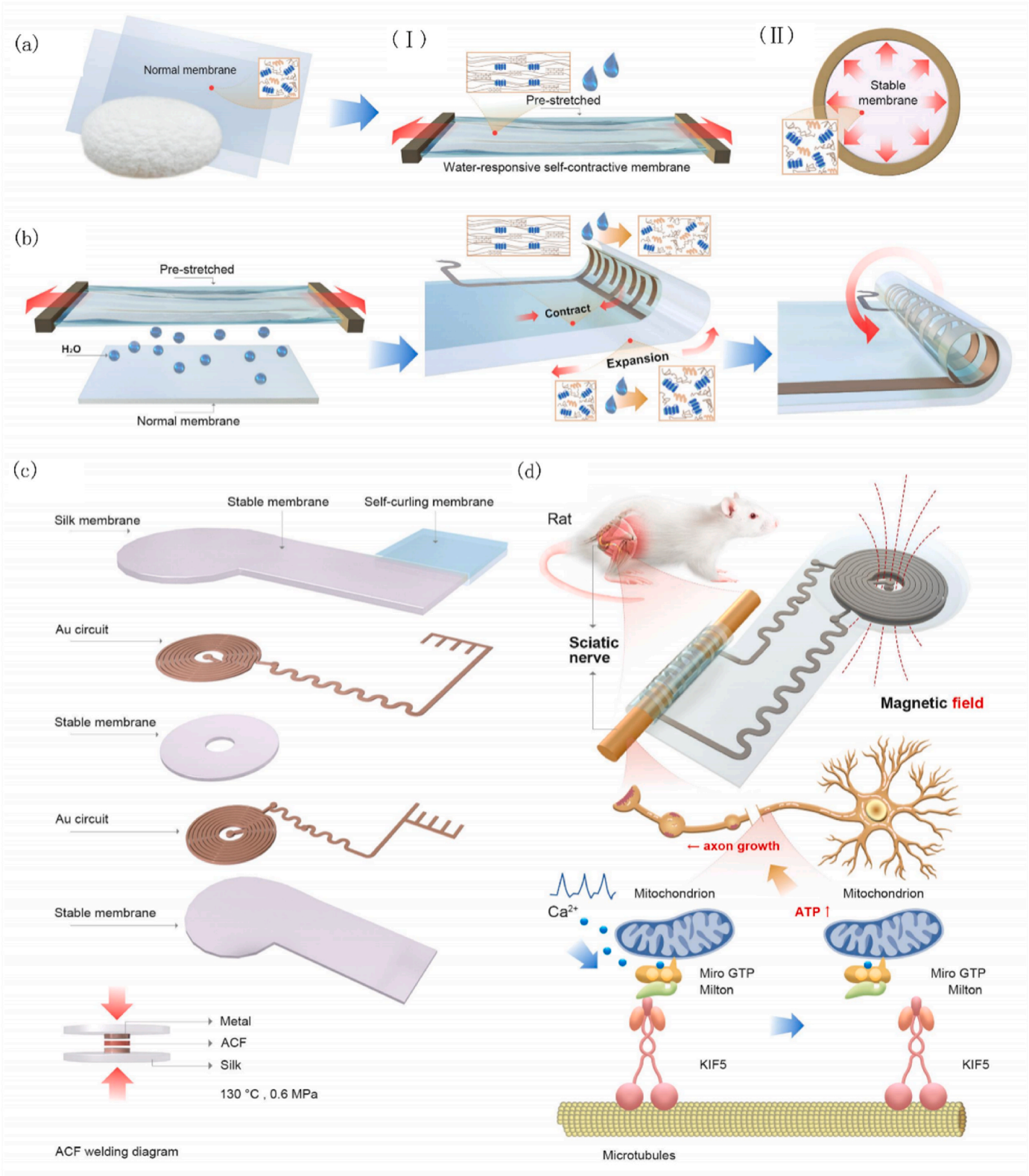

Fig. 1. Design of the SNGC- WES (a) Schematic detailing the fabrication of (I) water-responsive self-contractive membrane and (II) stable membrane. The process involves pre-stretching and fixing a cross-linked silk membrane to achieve self-contractile properties. (b) Schematic detailing the fabrication of the water-responsive self-curling silk membrane. The process involves immobilizing and cross-linking the water-responsive self-contractive membrane on top of the normal membrane. (c) Illustration of the device design. The wireless electrical stimulator comprises a magnetic fields harvester with inductive coils (Au, 1200 A thick) and an interlayer (silk, 50 μm), and a stimulation cuff (silk, 100 μm thick) with exposed electrodes for nerve interfacing. Assembly is accomplished through ACF welding and membrane cross-linking. (d) Schematic depicting wireless electric stimulation in a rat model and the potential mechanism for promoting axonal regeneration. The wireless receiver is subcutaneously placed, and the stimulation cuff, in contact with the sciatic nerve, promotes nerve regeneration by enhancing mitochondrial transport, ensuring the metabolically active region receives sufficient ATP for axonal regeneration. This is achieved by increasing axonal Ca^{2+} concentration, binding to Miro, and decoupling mitochondria from KIF5, arresting mitochondrial movement reversibly.

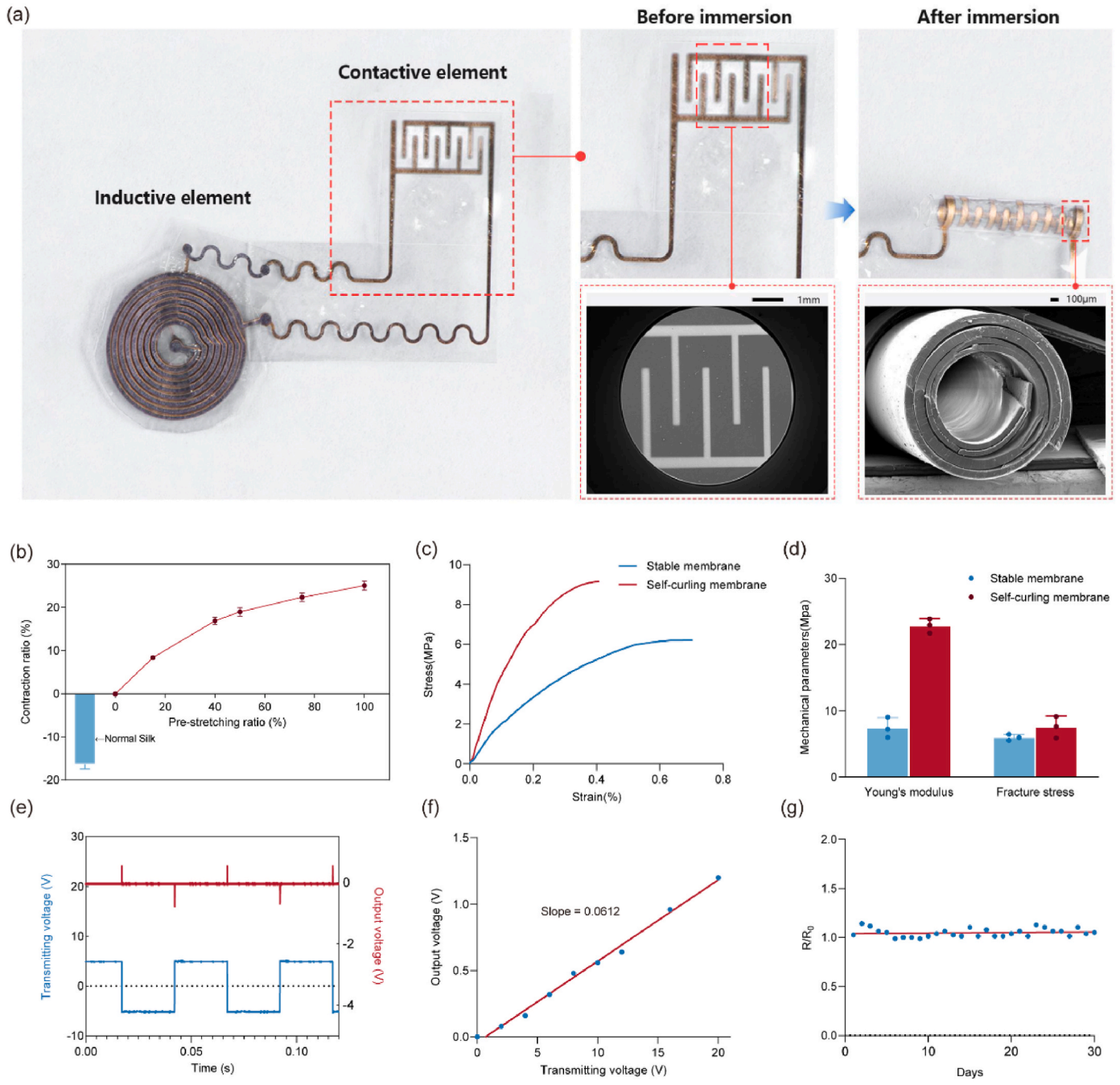

Fig. 2. Mechanical, electrical, and biological characterization of SNGC-WES (a) Snapshots of SNGC-WES, showing self-curling and membrane rolled into a cuff after immersion in deionized water. SEM images display metal lines on the membrane surface and self-curling bi-lateral membrane structure. (b) Contraction ratio of normal silk membrane and self-curling membrane. (c) Stress–strain curves for self-curling and stable membranes. (d) Mechanical parameters of self-curling and stable membranes. (e) Output waveform (red) wirelessly generated by an alternating current (square wave) applied to the transmission coil (transmitter, blue). n = 3 independent samples. (f) Correlation between output voltage and transmission voltage. (g) Changes in Au electrode resistance with immersion time in PBS (pH 7.4) at 37 °C.

1-month post-immersion in water. These results affirmed that SNGC-WES provides stable, controllable, and effective noninvasive electrical stimulation of nerves and operates successfully *in vivo* (Fig. 2g), presenting a significant advantage over electrical stimulators developed in previous studies [19,31,32,35,36].

3.2. Biological performance of SNGC-WES in vitro

Silk degradation primarily ensues through enzymatic processes. To examine SNGC-WES's biodegradability, we immersed it in a solution containing 0.1 mg/mL proteinase K at a constant 37 °C, and observed the near-complete degradation by day 7 (Fig. 3a and b). These results affirmed SNGC-WES's favorable biodegradation properties. DRG cells on the material's surface exhibited excellent adhesion, full extension (Fig. 3c and d), and high survival rates, as confirmed by live/dead cell staining (Fig. S4a). Assessing PC12 cell proliferation on the silk membranes through a CCK-8 assay, a common method in neurophysiological and neuropharmacological studies, revealed sustained proliferation on SNGC-WES for over 72 h, with a rate comparable to that on the silk membrane (Fig. 3e). Collectively, these results indicated SNGC-WES's

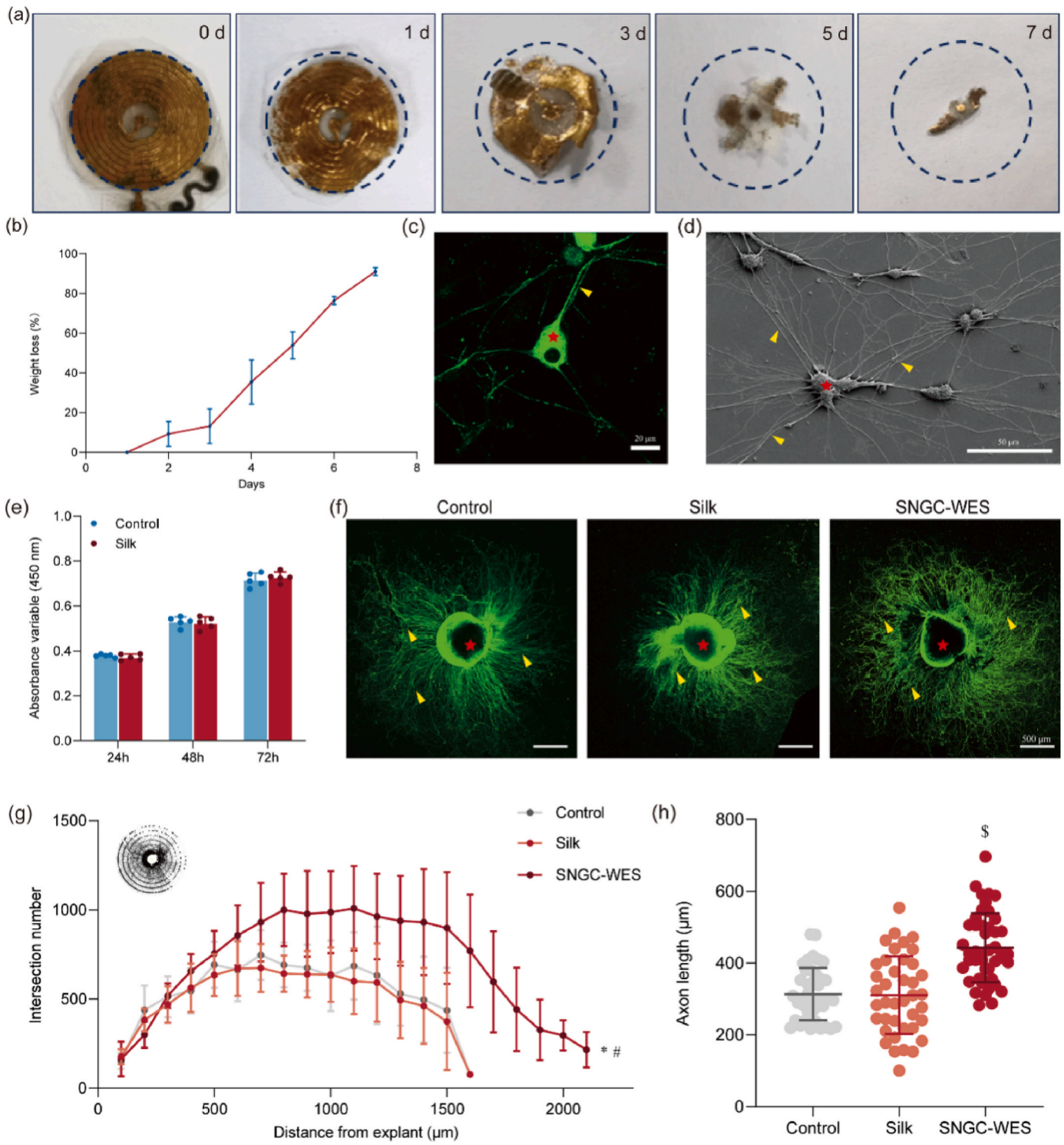

Fig. 3. Effectiveness of SNGC-WES in promoting axon growth (a) Images depicting accelerated dissolution of SNGC-WES in 0.1 mg/mL proteinase K solution at 37 °C. (b) Weight loss of SNGC-WES in 0.1 mg/mL proteinase K solution at 37 °C. (c) Immunofluorescence staining of DRG cells (β3-tubuling, green) on silk. Red asterisk: cytosol, yellow triangle: axon. (d) SEM image of DRG cells on silk. Red asterisk: cytosol, yellow triangles: axon. (e) Proliferation of PC12 cells cultured in material extract over 3 days (n = 5 per group). (f) Representative images of neural axon (β3-tubuling, green) outgrowth on materials. Red asterisks: DRG explants, yellow triangles: axon. (g) Sholl analysis of DRG explant axons with each concentric circle. n = 3 per group. *: $p < 0.05$ compared with Control group; #: $p < 0.05$ compared with silk group. (h) Quantitative analysis of axon length in DRG explants.

excellent biocompatibility, warranting further *in vitro* and *in vivo* experiments.

DRG explants on the standard silk membrane (Silk group) and SNGC-WES (SNGC-WES group) were compared to those cultured in confocal dishes (Control group). Immunofluorescence staining illustrated longer and denser axons in the SNGC-WES group, which received electrical stimulation (20 Hz, impulse, 100 mV/mm) for 3 days (Fig. 3f). Sholl analysis revealed a statistically significant increase in the SNGC-WES group compared to the control group (Fig. 3g, $P < 0.05$). Consistently, axon length measurement suggested that electrical stimulation

promotes axonal outgrowth, with DRG explants on SNGC-WES exhibiting significantly longer axons than other groups (Fig. 3h, $P < 0.05$). Similar phenomena were reported in prior studies, such as Brushart et al., who found brief electrical stimulation accelerated axonal growth [42,43]. These results imply that our constructed SNGC-WES fosters axon outgrowth *in vitro* and holds potential for peripheral nerve repair *in vivo*.

3.3. Functional and electrophysiological recovery in vivo

Upon confirming the *in vitro* efficacy of our system, we proceeded to assess the regenerative potential of SNGC-WES in a rat model with a surgically induced 10 mm gap defect in the sciatic nerve. Autografts or conduits were surgically affixed to the proximal and distal stumps of the transected sciatic nerve, with no occurrence of neuromas during the regeneration process (Fig. 4a). Importantly, no signs of local inflammation or systemic toxicity were observed in the animals (Figs. S4b and S4c). To further characterizing the biosafety of metals, we conducted histological sections using HE and VG staining on regenerative nerve samples. The staining results revealed that the metal did not trigger local inflammation, thus confirming its good biosafety (Fig. S5). To evaluate therapeutic benefits, we conducted functional and electrophysiological recovery assessments. Gait analysis, evaluating lower extremity motor function in rats, involved collecting hindfoot morphology and footprints (Fig. 4b). At three time points (4, 8, and 12 weeks), the SFI and SSI in the autograft and SNGC-WES groups significantly exceeded those in other groups (Fig. 4c, d, $P < 0.05$). Crucially, after 12 weeks, no statistically significant difference in SFI and SSI was observed between the autograft and SNGC-WES groups (Fig. 4c, d, $P > 0.05$).

Electrophysiological recovery was evaluated at 4, 8, and 12 weeks postoperatively. Fig. 4e presents representative CMAP records of the operative limb. Analysis revealed a noteworthy increase in the mean peak amplitude of CMAP in both the autograft and SNGC-WES groups at 12 weeks post-surgery (Fig. 4f, $P < 0.05$). In Fig. 4g, the mean latencies of CMAPs in the autograft and SNGC-WES groups were shorter than those in the control group ($P < 0.05$). Prolonged latencies signify inferior recovery in electrophysiology. Additionally, the mean conduction velocity of CMAPs in the autograft and SNGC-WES groups exceeded that in the control group (Fig. 4h, $P < 0.05$). No statistically significant difference in electrophysiological parameters was observed between the SNGC-WES and autograft groups at 12 weeks postoperatively ($P > 0.05$). Overall, the data lend support to the hypothesis that SNGC-WES effectively fosters neurophysiological recovery through electrical stimulation.

Having confirmed the remarkable efficacy of SNGC-WES in promoting neurophysiological recovery, our focus shifted to assessing the structural integrity of the gastrocnemius muscle following treatment. The sciatic nerve bifurcates into the tibial nerve, responsible for innervating the gastrocnemius muscle. Muscle atrophy is closely associated with denervation time [44]. As illustrated in Fig. 5a, gastrocnemius muscle atrophy was less pronounced in the autograft and SNGC-WES groups. Quantitative analysis of wet gastrocnemius muscle collected at the 12-week mark revealed a substantial improvement in relative muscle weight recovery (normalized to the contralateral uninjured side) in the autograft and SNGC-WES groups, compared to the control and conduit groups ($P < 0.05$, Fig. S6a). Furthermore, no significant difference was observed between the SNGC-WES and autograft groups in muscle wet weight ($P > 0.05$). To further elucidate the impact of our interventions, gastrocnemius muscle was stained with Masson's dye, and the muscle fiber cross-sectional area and collagen fiber area percentage in the four experimental groups were analyzed (Fig. 5c and d). In comparison to the control and conduit groups, the muscle fiber cross-sectional areas in the autograft and SNGC-WES groups were significantly larger ($P < 0.05$). Conversely, the collagen fiber area percentage in the autograft and SNGC-WES groups was markedly smaller ($P < 0.05$). Meanwhile, there was no significant difference in muscle fiber cross-sectional area and collagen fiber area percentage between the autograft group and SNGC-WES group ($P > 0.05$). These data affirmed that SNGC-WES effectively expedites muscle reinnervation through electrical stimulation.

3.4. Morphological recovery of the transected sciatic nerve

In conjunction with the noteworthy functional recovery, histological analyses provided additional evidence of robust nerve regeneration. The efficacy of nerve remediation was assessed through NF200 and S100 staining, with NF200 serving as a specific biomarker for axonal neurofilament, and S100 as a biomarker for Schwann cells. Fluorescence images depicted orderly arrangements of regenerated axons and Schwann cells in both the autograft and SNGC-WES groups (Fig. 6a). In contrast, the control group exhibited sparse and disorderly fluorescence distribution of axons and Schwann cells. Notably, the SNGC-WES group demonstrated significantly greater fluorescence distribution than the control and conduit groups, albeit slightly less than the autograft group. The mean percentages of NF200/S100 positive staining in both autograft and SNGC-WES groups were higher than in the other groups ($P < 0.05$), with no significant difference observed between the autograft and SNGC-WES groups (Fig. 6b and c). Images of HE staining also showed the same results (Fig. S6b).

Detailed examination of the myelinated nerve fibers in the middle segments of the regenerated nerves is presented in Fig. 6d. At 12 weeks postoperatively, all groups exhibited newly generated myelinated nerve fibers. Autograft and SNGC-WES groups displayed normally and evenly distributed axons and myelin sheaths, accompanied by Schwann cells exhibiting favorable morphology. In contrast, the conduit group exhibited significant variations in myelin sheath size, with increased fibroblast infiltration and the presence of unmyelinated and hypomyelinated axons. The SNGC-WES group demonstrated superior percentages of total area and diameter of myelinated axons compared to the control and conduit groups ($P < 0.05$), comparable to those of the Autograft group at week 12 ($P > 0.05$) (Fig. 6e and f). The thickness of the myelin sheath was also significantly higher in the SNGC-WES group than in the control and conduit groups ($P < 0.05$) (Fig. 6g). The scatter plots distribution of g-ratio analysis revealed that the g-ratio values in the autograft and SNGC-WES groups were close to 0.6, consistent with the values found in healthy nerves. In summary, newborn peripheral nerves in SNGC-WES exhibited a restored microstructure, well-oriented axon regeneration, and Schwann cell myelination comparable to the gold-standard autograft group, contributing to the significant functional recovery.

3.5. SNGC-WES promotes axonal regeneration involving signaling pathways associated with mitochondrial movement

Unveiling the potential mechanism governing the promotion of axonal outgrowth through electrical stimulation, we conducted RNA sequencing on DRG samples from both the standard silk group and the SNGC-WES group. The volcanic plot of DEGs displayed 773 upregulated DEGs and 460 downregulated DEGs in the SNGC-WES group (Fig. 7a). A more granular analysis of the sequencing data via GO enrichment illuminated distinct biological functions regulated in the SNGC-WES group, predominantly associated with diverse developmental processes (Fig. 7b). We delved deeper into the exploration of key signaling pathways implicated in nerve repair through KEGG enrichment analysis. Notably, calcium signaling pathways and metabolic pathways emerged as prominently upregulated (Fig. 7c). Previous studies suggested that these pathways may contribute to nerve regeneration by enhancing anterograde mitochondrial transport [45]. Crucially, anterograde transport of mitochondria plays a pivotal role in supplying the distal sites of neuronal processes with these cellular powerhouses, ensuring a sufficient Adenosine 5′-triphosphate (ATP) supplies essential for neuron growth, survival, and regeneration [46]. Neurons, when injured, require

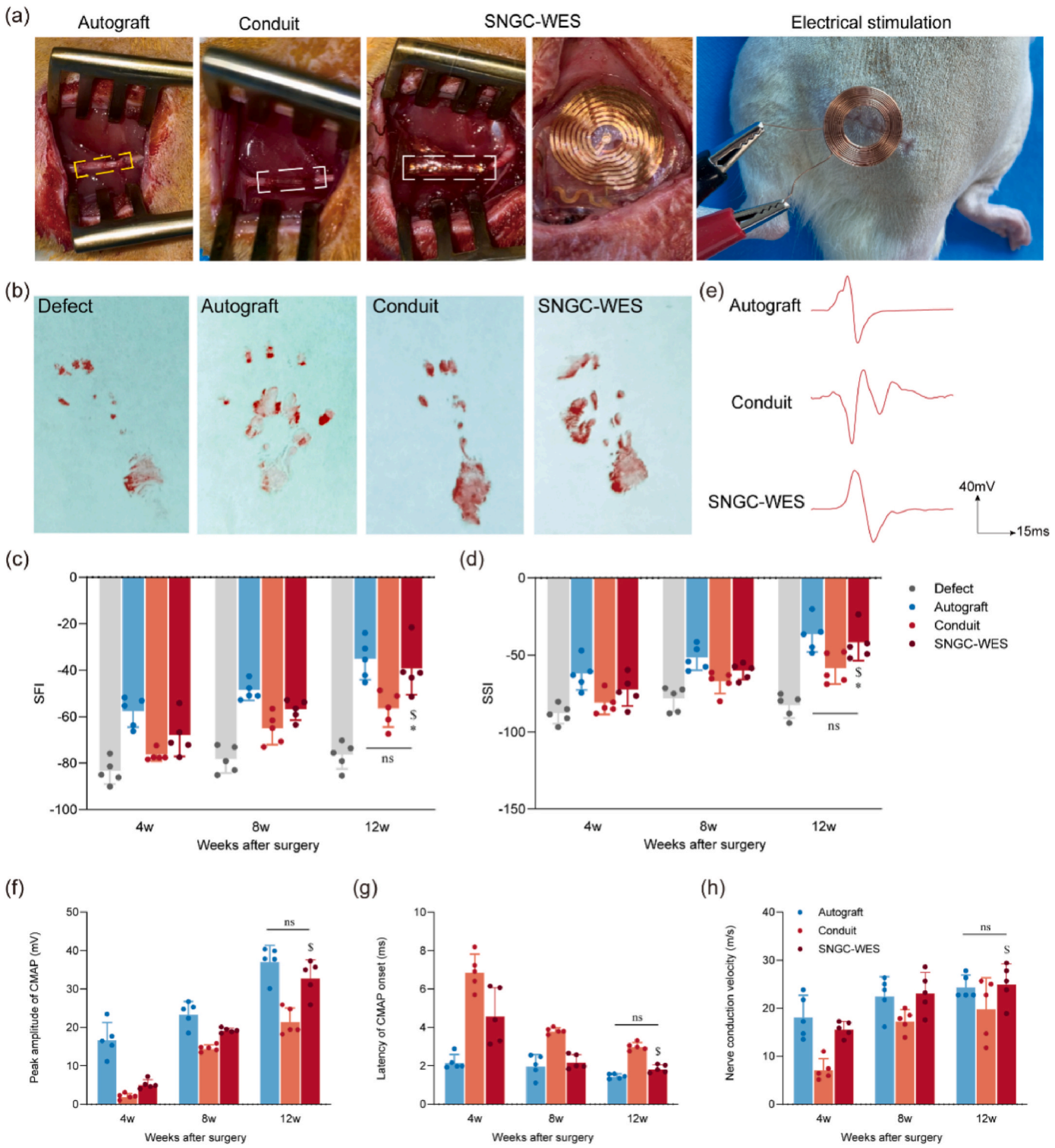

Fig. 4. Surgical implantation, operation of SNGC-WES, and *in vivo* functional recovery of the regenerated sciatic nerve (a) Schematic illustration of surgical implantation and SNGC-WES operation. Left to right: Autologous nerve graft, simple silk conduit, SNGC-WES (Left: cuff with exposed electrodes around nerve stumps; Right: inductive coils under the skin), and stimulation operation (activated with a transmitting coil). (b) Representative images of walking track footprints at 12 weeks postoperatively. (c, d) Quantification of sciatic nerve function index (SFI) and static sciatic index (SSI) at 4-, 8-, and 12-weeks post-implantation. (e) Representative images of CAMPs recorded on the gastrocnemius muscle. (f) Peak amplitude of CMAP, (g) latency of CMAP onset, and (h) conduction velocity at 4-, 8-, and 12-weeks post-implantation. Data presented as mean ± SD, n = 5 per group (C, D, F–H). *: $p < 0.05$ compared with Defect group; #: $p < 0.05$ compared with Autograft group; $: $p < 0.05$ compared with Conduit group.

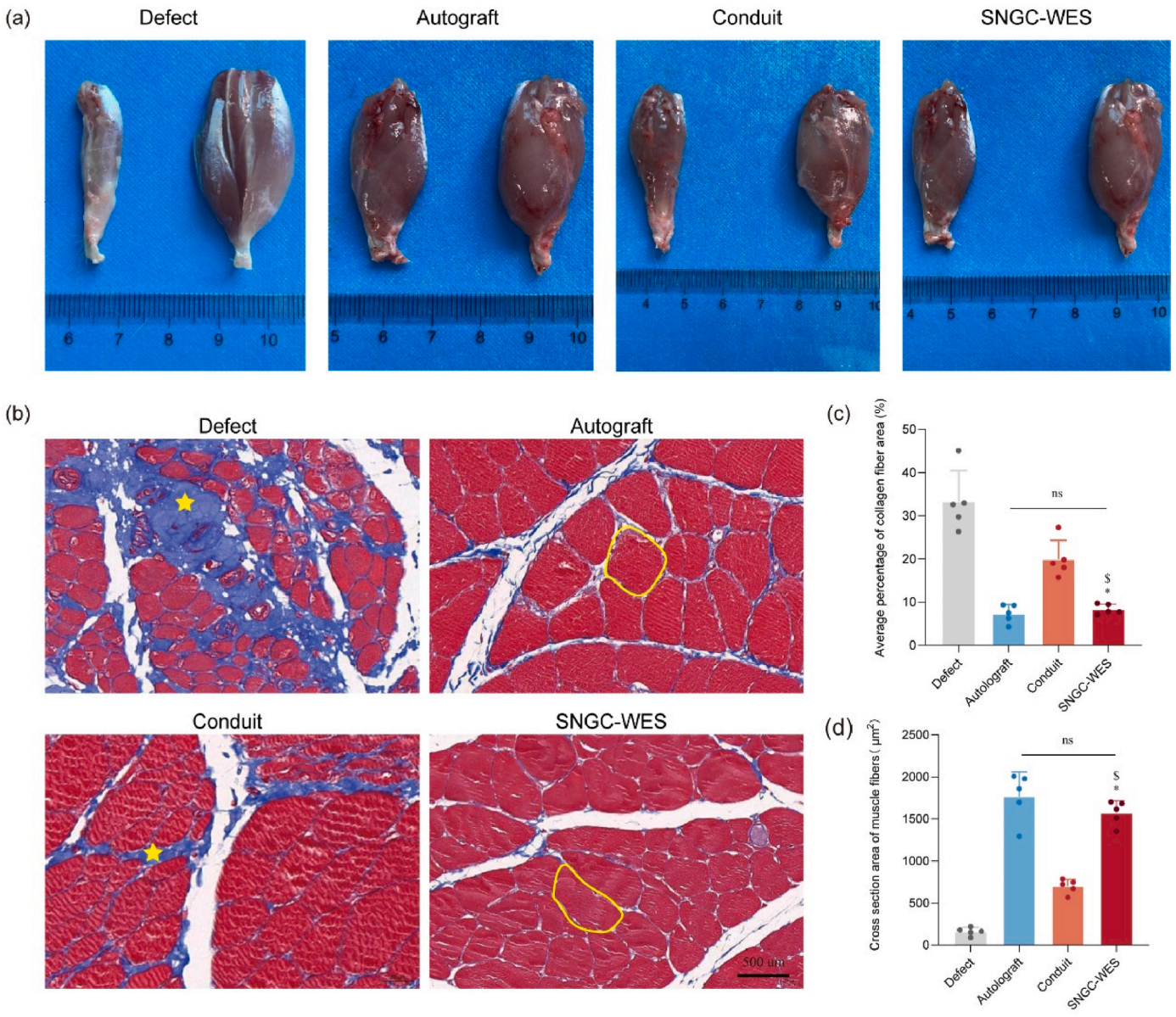

Fig. 5. Histological assessment of gastrocnemius muscles (a) Images comparing gastrocnemius muscle between normal and operative sides. (b) Masson's trichrome staining of cross sections showing fibrotic areas (yellow asterisks) and muscle fibers (yellow wireframes). (c) Quantification of average collagen fiber area percentage. (d) Quantification of cross-sectional area of muscle fibers. Data presented as mean ± SD, n = 5 per group (c–d). *: $p < 0.05$ compared with Defect group; #: $p < 0.05$ compared with Autograft group; $: $p < 0.05$ compared with Conduit group.

rapid remodeling into active growth cones, a process demanding substantial energy. The proper translocation of mitochondria to the site of axonal injury guarantees that the metabolically active region receives adequate ATP to foster axonal regeneration [47]. This transport is facilitated by a microtubule-based adaptor or motor proteins trafficking system, comprising KIF5 (motor), Milton (adaptor), Miro (mitochondrial receptor protein), and syntabulin (Snph) [48].

Significantly, the SNGC-WES group exhibited upregulated expression of genes related to mitochondrion transport (including *Aif1*, *Kif19*, *Kif9*, *Kifc2*, *Sema7a*, *Snph*, and *Tubb3*) and biomarkers associated with neuron regeneration (including *Metrn*, *Nefh*, and *Nrep*) (Fig. 7d). To corroborate these RNA sequencing results, we conducted qRT-PCR and WB analyses. qRT-PCR results affirmed elevated gene levels of *Kif5B*, *Miro1*, *Snph*, *Tubb3*, *NGF*, and *MBP* (Fig. 7e). Additionally, WB analysis demonstrated increased expression of several proteins related to mitochondrion transport (KHC, Kif5B, Snph, and Miro1) (Fig. 7f). Further elucidation of the mitochondrial transport process involved immunofluorescence staining, revealing a higher number of mitochondria in the axons of DRG cells in the SNGC-WES group compared to the standard silk group (Fig. 7g and h). Time-lapse imaging and kymograph analysis illustrated a substantial increase in axonal mitochondrial transport (Fig. 7i). Cytosolic Ca^{2+} can bind to Miro and decouple mitochondria from KIF5, leading to reversible arrest of mitochondrial movement. Thus, mitochondria recruitment are more likely appeared to be influenced by cytosolic Ca^{2+}, as demonstrated by increased Ca^{2+} concentration in axons after electrical stimulation (Fig. 7j, Fig. S7) [49]. In summary, SNGC-WES facilitates peripheral nerve regeneration by enhancing the anterograde transport of mitochondria, involving increased axonal Ca^{2+} concentration and the upregulation of mitochondrial anterograde transport-related gene and protein expression (Fig. 1d).

As with the majority of studies, the design of the current study is subject to limitations. The first is that our study did not delve deeply into the intricacies of frequency matching. Although the experimental results

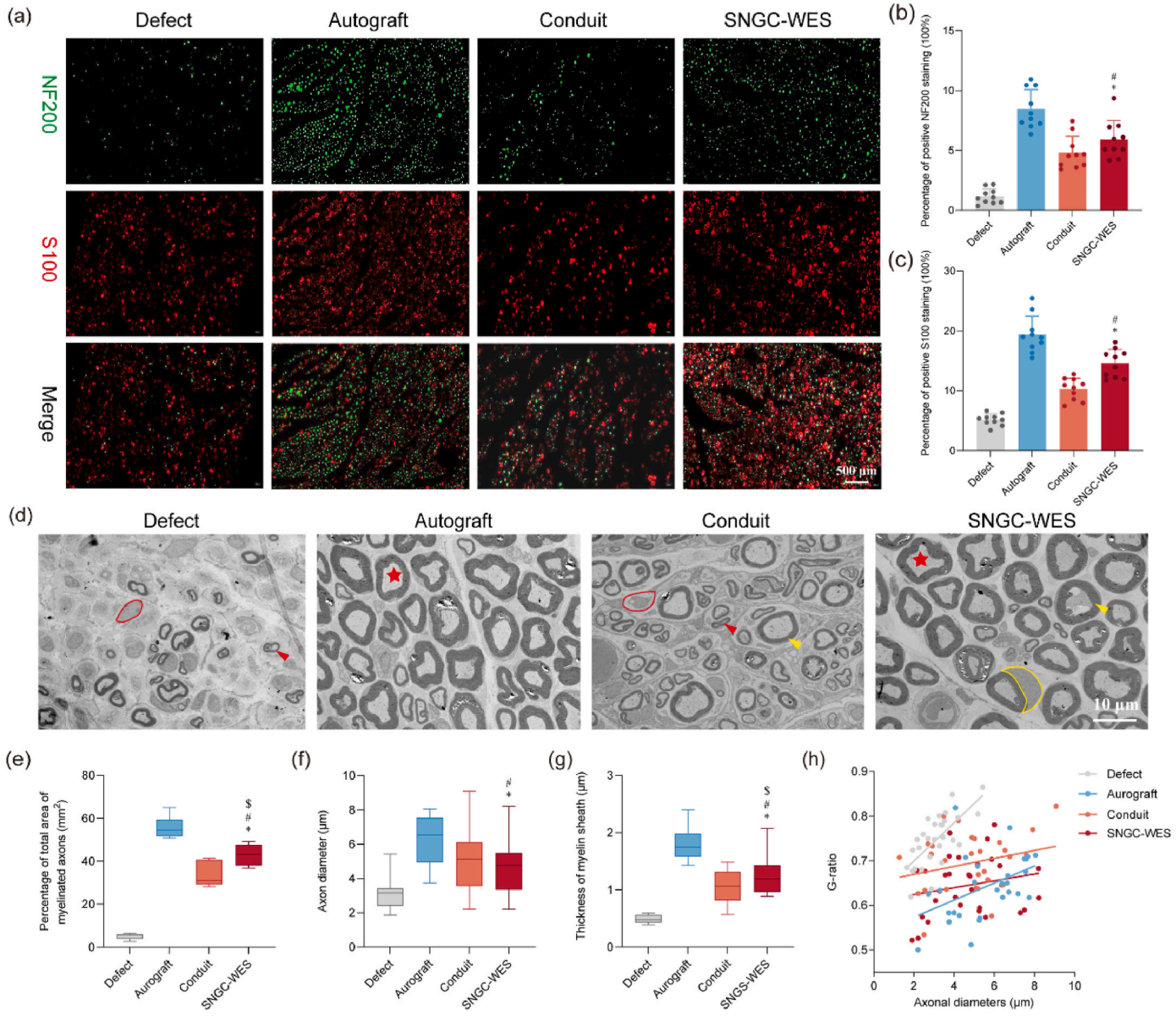

Fig. 6. Immunohistochemical staining and transmission electron micrographs of regenerated nerves (a) Representative immunofluorescence staining images of cross-sections of regenerated nerves. Axons are denoted by green fluorescence (NF200), while Schwann cells are marked with red fluorescence (S100). (b) Percentage of positive NF200 staining. (c) Percentage of positive S100 staining. (d) Transmission electron micrographs of regenerated nerves at 12 weeks post-implantation. Red wireframes indicate unclassified axons, red asterisks denote normal axons, yellow arrowheads represent normal myelination, red arrowheads signify hypomyelination, and yellow wireframes depict Schwann cells. (e) Quantification of the percentage of the total area occupied by myelinated axons. (f) Quantification of axon diameter. (g) Quantification of the thickness of the myelin sheath. (h) Scatter plot for the g-ratio in the indicated groups at 12 weeks post-implantation. Partial data are presented as bar charts with mean ± SD, n = 5 per group (b, c), while another part of the data is depicted as box diagrams with mean ± SD, n = 5 per group (e–g). *: $p < 0.05$ compared with the Defect group; #: $p < 0.05$ compared with the Autograft group; $: $p < 0.05$ compared with the Conduit group.

show that the device can promote nerve repair by wirelessly transmitting electrical stimulation, it is undeniable that the transmission is relatively inefficient. This limits the future clinical application of the system. The second limitation concerns that we ignore the effect of electrical stimulation on phagocyte behavior. Phagocytosis involves a process of degradation of silk protein material, potentially affecting the length of the device's operating time. In further research, we will explore these two aspects in depth and improve the device.

4. Conclusion

In this study, we developed a SNGC-WES designed to bridge a 10-mm gap in a rat sciatic nerve defect model. Remarkably, this conduit exhibited a notable improvement in both axonal regeneration and functional recovery. These observed outcomes not only rivaled those achieved with autografts but also surpassed the reparative efficacy of traditional silk conduits. Furthermore, our findings suggest that SNGC-WES promotes axon regeneration by enhancing mitochondrial anterograde transport. Taken together, these results highlight the considerable potential of SNGC-WES as a promising alternative to autografts for the repair of peripheral nerve defects.

Ethics approval and consent to participate

The Fourth Military Medical University Animal Research Ethics Committee's guiding principles (Protocol Number: 20230084) were

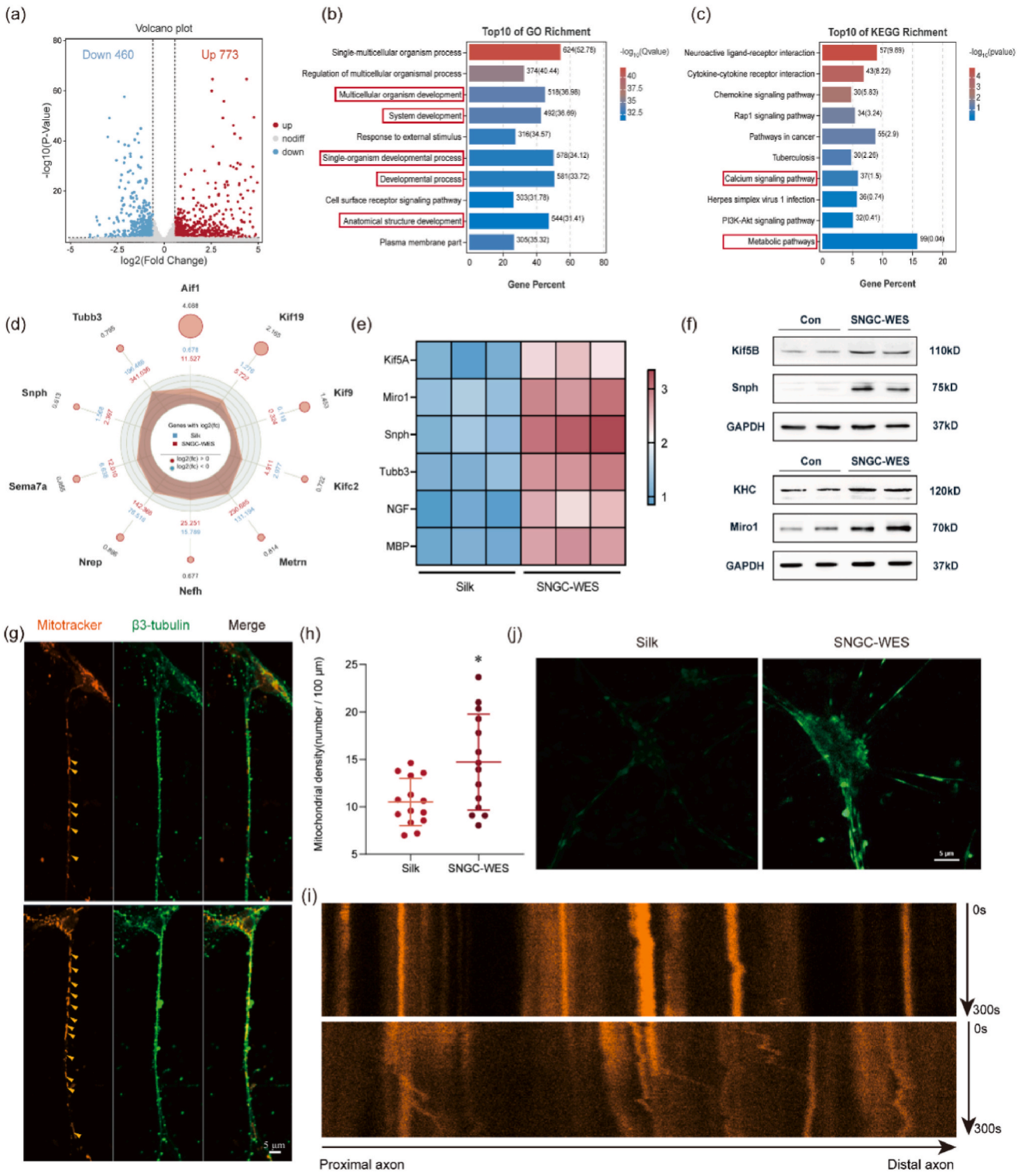

Fig. 7. Transcriptome profiles of axon outgrowth driven by SNGC-WES and characterization of mitochondrial motility (a) Volcano map of DEGs in DRGs comparing SNGC-WES to silk conduit. Red dots indicate significantly upregulated DEGs, blue dots indicate significantly downregulated DEGs, and grey dots indicate no significance. (b) Top 10 GO terms. Key terms are marked by red rectangular boxes. (c) KEGG pathway enrichment. Key processes and pathways are marked by red rectangular boxes. (d) Radargram of key DEGs in DRGs comparing SNGC-WES to silk conduit. The numbers in the outermost circle represent log2(FC) values. Red circles indicate significantly upregulated DEGs. The blue and red data in circle 3 represent the mean expression values for samples. Irregular shapes represent the expression abundance of samples on each axis. (e) Heatmap of mRNA expression results of DRGs comparing SNGC-WES to silk conduit after electrical stimuli for 5 days. (f) Expression of key proteins in DRG cells comparing SNGC-WES to silk conduit. (g) Representative images of mitochondria (Mitotracker, red) distribution in DRG axons (β3-tubulin, green). Yellow triangles denote mitochondria. (h) Quantitative analysis of axonal mitochondrial density. (i) Time-lapse image of axonal mitochondria for a total of 100 frames with 3 s intervals. (j) Intracellular Ca^{2+} levels monitored by labeling with Fluo-4, AM. ns: $P \geq 0.05$; *: $P < 0.05$; **: $P < 0.01$ (d, f).

followed in all experiments.

Declaration of competing interest

The authors declare that they have no known competing financial interests or personal relationships that could have appeared to influence the work reported in this paper.

CRediT authorship contribution statement

Hao Bai: Writing – original draft, Validation, Methodology, Investigation, Conceptualization. **Siqi Zhang:** Writing – original draft, Visualization, Validation, Methodology, Investigation. **Huiran Yang:** Visualization, Validation, Methodology, Conceptualization. **Jing Wang:** Visualization, Validation, Investigation. **Hongli Chen:** Validation, Methodology. **Jia Li:** Validation, Methodology. **Lin Li:** Validation, Methodology. **Qian Yang:** Validation, Methodology. **Bo Peng:** Writing – review & editing. **Ziyi Zhu:** Validation, Methodology. **Siyuan Ni:** Validation, Methodology. **Keyin Liu:** Writing – review & editing, Validation, Methodology, Investigation. **Wei Lei:** Writing – review & editing, Supervision, Project administration, Funding acquisition, Conceptualization. **Tiger H. Tao:** Writing – review & editing, Supervision, Project administration. **Yafei Feng:** Writing – review & editing, Project administration, Funding acquisition, Conceptualization.

Acknowledgements

This work was supported by the National Natural Science Foundation of China (82172476, 82172393).

Appendix A. Supplementary data

Supplementary data to this article can be found online at https://doi.org/10.1016/j.bioactmat.2024.05.033.

References

[1] L.R. Robinson, Traumatic injury to peripheral nerves, Muscle Nerve 66 (6) (2022) 661–670, https://doi.org/10.1002/mus.27706.
[2] J. Wang, H. Xiong, T. Zhu, Y. Liu, H. Pan, C. Fan, X. Zhao, W.W. Lu, Bioinspired Multichannel nerve guidance conduit based on shape memory nanofibers for potential application in peripheral nerve repair, ACS Nano 14 (10) (2020) 12579–12595, https://doi.org/10.1021/acsnano.0c03570.
[3] H. Xie, W. Yang, J. Chen, J. Zhang, X. Lu, X. Zhao, K. Huang, H. Li, P. Chang, Z. Wang, L. Wang, A silk sericin/silicone nerve guidance conduit promotes regeneration of a transected sciatic nerve, Adv. Healthcare Mater. 4 (15) (2015) 2195–2205, https://doi.org/10.1002/adhm.201500355.
[4] X.N. Yang, Y.Q. Jin, H. Bi, W. Wei, J. Cheng, Z.Y. Liu, Z. Shen, Z.L. Qi, Y. Cao, Peripheral nerve repair with epimysium conduit, Biomaterials 34 (22) (2013) 5606–5616, https://doi.org/10.1016/j.biomaterials.2013.04.018.
[5] G. Hussain, J. Wang, A. Rasul, H. Anwar, M. Qasim, S. Zafar, N. Aziz, A. Razzaq, R. Hussain, J.G. De Aguilar, T. Sun, Current status of therapeutic approaches against peripheral nerve injuries: a detailed story from injury to recovery, Int. J. Biol. Sci. 16 (1) (2020) 116–134, https://doi.org/10.7150/ijbs.35653.
[6] T. Baudequin, M. Tabrizian, Multilineage constructs for scaffold-based tissue engineering: a review of tissue-specific challenges, Adv. Healthcare Mater. 7 (3) (2018), https://doi.org/10.1002/adhm.201700734.
[7] S. Yi, L. Xu, X. Gu, Scaffolds for peripheral nerve repair and reconstruction, Exp. Neurol. 319 (2019) 112761, https://doi.org/10.1016/j.expneurol.2018.05.016.
[8] A. Wubneh, E.K. Tsekoura, C. Ayranci, H. Uludag, Current state of fabrication technologies and materials for bone tissue engineering, Acta Biomater. 80 (2018) 1–30, https://doi.org/10.1016/j.actbio.2018.09.031.
[9] A. Magaz, A. Faroni, J.E. Gough, A.J. Reid, X. Li, J.J. Blaker, Bioactive silk-based nerve guidance conduits for augmenting peripheral nerve repair, Adv. Healthcare Mater. 7 (23) (2018) e1800308, https://doi.org/10.1002/adhm.201800308.
[10] L. Guo, Z. Liang, L. Yang, W. Du, T. Yu, H. Tang, C. Li, H. Qiu, The role of natural polymers in bone tissue engineering, J. Contr. Release 338 (2021) 571–582, https://doi.org/10.1016/j.jconrel.2021.08.055.
[11] M. Aoki, Y. Masuda, K. Ishikawa, Y. Tamada, Fractionation of regenerated silk fibroin and characterization of the fractions, Molecules 26 (20) (2021), https://doi.org/10.3390/molecules26206317.
[12] M. Floren, C. Migliaresi, A. Motta, Processing techniques and applications of silk hydrogels in bioengineering, J. Funct. Biomater. 7 (3) (2016), https://doi.org/10.3390/jfb7030026.
[13] J. Hua, R. Huang, Y. Huang, S. Yan, Q. Zhang, Comparison of silk hydrogels prepared via different methods, Polymers 15 (22) (2023), https://doi.org/10.3390/polym15224419.
[14] Y. Zhao, Z.S. Zhu, J. Guan, S.J. Wu, Processing, mechanical properties and bio-applications of silk fibroin-based high-strength hydrogels, Acta Biomater. 125 (2021) 57–71, https://doi.org/10.1016/j.actbio.2021.02.018.
[15] G. Xiang, K. Liu, T. Wang, X. Hu, J. Wang, Z. Gao, W. Lei, Y. Feng, T.H. Tao, In situ regulation of macrophage polarization to enhance osseointegration under diabetic conditions using injectable silk/sitagliptin gel scaffolds, Adv. Sci. 8 (3) (2021) 2002328, https://doi.org/10.1002/advs.202002328.
[16] T. Wang, K. Liu, J. Wang, G. Xiang, X. Hu, H. Bai, W. Lei, T.H. Tao, Y. Feng, Spatiotemporal regulation of injectable heterogeneous silk gel scaffolds for accelerating guided vertebral repair, Adv. Healthcare Mater. 12 (7) (2023) e2202210, https://doi.org/10.1002/adhm.202202210.
[17] A. Alessandrino, F. Fregnan, M. Biagiotti, L. Muratori, G.A. Bassani, G. Ronchi, V. Vincoli, P. Pierimarchi, S. Geuna, G. Freddi, SilkBridge: a novel biomimetic and biocompatible silk-based nerve conduit, Biomater. Sci. 7 (10) (2019) 4112–4130, https://doi.org/10.1039/c9bm00783k.
[18] Y. Qian, H. Lin, Z.W. Yan, J.L. Shi, C.Y. Fan, Functional nanomaterials in peripheral nerve regeneration: scaffold design, chemical principles and microenvironmental remodeling, Mater. Today 51 (2021) 165–187, https://doi.org/10.1016/j.mattod.2021.09.014.
[19] J.B. Senger, K.N. Rabey, M.J. Morhart, K.M. Chan, C.A. Webber, Conditioning electrical stimulation accelerates regeneration in nerve transfers, Ann. Neurol. 88 (2) (2020) 363–374, https://doi.org/10.1002/ana.25796.
[20] J. Du, G. Zhen, H. Chen, S. Zhang, L. Qing, X. Yang, G. Lee, H.Q. Mao, X. Jia, Optimal electrical stimulation boosts stem cell therapy in nerve regeneration, Biomaterials 181 (2018) 347–359, https://doi.org/10.1016/j.biomaterials.2018.07.015.
[21] Y. Zhang, S. Chen, Z. Xiao, X. Liu, C. Wu, K. Wu, A. Liu, D. Wei, J. Sun, L. Zhou, H. Fan, Magnetoelectric nanoparticles incorporated biomimetic matrix for wireless electrical stimulation and nerve regeneration, Adv. Healthcare Mater. 10 (16) (2021) e2100695, https://doi.org/10.1002/adhm.202100695.
[22] X. Li, T. Zhang, C. Li, W. Xu, Y. Guan, X. Li, H. Cheng, S. Chen, B. Yang, Y. Liu, Z. Ren, X. Song, Z. Jia, Y. Wang, J. Tang, Electrical stimulation accelerates Wallerian degeneration and promotes nerve regeneration after sciatic nerve injury, Glia 71 (3) (2023) 758–774, https://doi.org/10.1002/glia.24309.
[23] J. Huang, X. Hu, L. Lu, Z. Ye, Y. Wang, Z. Luo, Electrical stimulation accelerates motor functional recovery in autograft-repaired 10 mm femoral nerve gap in rats, J. Neurotrauma 26 (10) (2009) 1805–1813, https://doi.org/10.1089/neu.2008.0732.
[24] D. Lal, L.T. Hetzler, N. Sharma, R.D. Wurster, S.J. Marzo, K.J. Jones, E. M. Foecking, Electrical stimulation facilitates rat facial nerve recovery from a crush injury, Otolaryngol. Head Neck Surg. 139 (1) (2008) 68–73, https://doi.org/10.1016/j.otohns.2008.04.030.
[25] X.L. Chu, X.Z. Song, Q. Li, Y.R. Li, F. He, X.S. Gu, D. Ming, Basic mechanisms of peripheral nerve injury and treatment via electrical stimulation, Neural Regen Res 17 (10) (2022) 2185–2193, https://doi.org/10.4103/1673-5374.335823.
[26] A.L. O'brien, J.M. West, T.M. Saffari, M. Nguyen, A.M. Moore, Promoting nerve regeneration: electrical stimulation, gene therapy, and beyond, Physiology 37 (6) (2022), https://doi.org/10.1152/physiol.00008.2022.
[27] J. Zhang, M. Li, E.T. Kang, K.G. Neoh, Electrical stimulation of adipose-derived mesenchymal stem cells in conductive scaffolds and the roles of voltage-gated ion channels, Acta Biomater. 32 (2016) 46–56, https://doi.org/10.1016/j.actbio.2015.12.024.
[28] T. Gordon, Electrical stimulation to enhance axon regeneration after peripheral nerve injuries in animal models and humans, Neurotherapeutics 13 (2) (2016) 295–310, https://doi.org/10.1007/s13311-015-0415-1.
[29] Y. Qian, W.E. Yuan, Y. Cheng, Y. Yang, X. Qu, C. Fan, Concentrically integrative bioassembly of a three-dimensional black phosphorus nanoscaffold for restoring neurogenesis, angiogenesis, and immune homeostasis, Nano Lett. 19 (12) (2019) 8990–9001, https://doi.org/10.1021/acs.nanolett.9b03980.
[30] M. Sajic, V. Mastrolia, C.Y. Lee, D. Trigo, M. Sadeghian, A.J. Mosley, N.A. Gregson, M.R. Duchen, K.J. Smith, Impulse conduction increases mitochondrial transport in adult mammalian peripheral nerves in vivo, PLoS Biol. 11 (12) (2013) e1001754, https://doi.org/10.1371/journal.pbio.1001754.
[31] L. Wang, C. Lu, S. Yang, P. Sun, Y. Wang, Y. Guan, S. Liu, D. Cheng, H. Meng, Q. Wang, J. He, H. Hou, H. Li, W. Lu, Y. Zhao, J. Wang, Y. Zhu, Y. Li, D. Luo, T. Li, H. Chen, S. Wang, X. Sheng, W. Xiong, X. Wang, J. Peng, L. Yin, A fully biodegradable and self-electrified device for neuroregenerative medicine, Sci. Adv. 6 (50) (2020), https://doi.org/10.1126/sciadv.abc6686.
[32] B. Ferrigno, R. Bordett, N. Duraisamy, J. Moskow, M.R. Arul, S. Rudraiah, S. P. Nukavarapu, A.T. Vella, S.G. Kumbar, Bioactive polymeric materials and electrical stimulation strategies for musculoskeletal tissue repair and regeneration, Bioact. Mater. 5 (3) (2020) 468–485, https://doi.org/10.1016/j.bioactmat.2020.03.010.
[33] Y. Qian, Y. Cheng, J. Song, Y. Xu, W.E. Yuan, C. Fan, X. Zheng, Mechano-informed biomimetic polymer scaffolds by incorporating self-powered zinc oxide nanogenerators enhance motor recovery and neural function, Small 16 (32) (2020) e2000796, https://doi.org/10.1002/smll.202000796.
[34] Y. Qian, Y. Xu, Z.W. Yan, Y. Jin, X. Chen, W.E. Yuan, C.Y. Fan, Boron nitride nanosheets functionalized channel scaffold favors microenvironment rebalance cocktail therapy for piezocatalytic neuronal repair, Nano Energy 83 (2021). ARTN105779.10.1016/j.nanoen.2021.105779.
[35] Y. Sun, Q. Quan, H. Meng, Y. Zheng, J. Peng, Y. Hu, Z. Feng, X. Sang, K. Qiao, W. He, X. Chi, L. Zhao, Enhanced neurite outgrowth on a multiblock conductive

nerve scaffold with self-powered electrical stimulation, Adv. Healthcare Mater. 8 (10) (2019) e1900127, https://doi.org/10.1002/adhm.201900127.
[36] Y.S. Choi, Y.Y. Hsueh, J. Koo, Q. Yang, R. Avila, B. Hu, Z. Xie, G. Lee, Z. Ning, C. Liu, Y. Xu, Y.J. Lee, W. Zhao, J. Fang, Y. Deng, S.M. Lee, A. Vazquez-Guardado, I. Stepien, Y. Yan, J.W. Song, C. Haney, Y.S. Oh, W. Liu, H.J. Yoon, A. Banks, M. R. Macewan, G.A. Ameer, W.Z. Ray, Y. Huang, T. Xie, C.K. Franz, S. Li, J.A. Rogers, Stretchable, dynamic covalent polymers for soft, long-lived bioresorbable electronic stimulators designed to facilitate neuromuscular regeneration, Nat. Commun. 11 (1) (2020) 5990, https://doi.org/10.1038/s41467-020-19660-6.
[37] H. Tao, S.W. Hwang, B. Marelli, B. An, J.E. Moreau, M.M. Yang, M.A. Brenckle, S. Kim, D.L. Kaplan, J.A. Rogers, F.G. Omenetto, Silk-based resorbable electronic devices for remotely controlled therapy and in vivo infection abatement, P Natl Acad Sci USA 111 (49) (2014) 17385–17389, https://doi.org/10.1073/pnas.1407743111.
[38] H.R. Yang, Z.Y. Zhu, X.Y. Wang, D.J. Zou, W.Q. Jiang, Z.T. Zhou, L.Y. Sun, K.Y. Liu, H. Tao, X.L. Wei, Oriented crystallization silk-based electronic interface towards chronical recording. Presented at 2024 IEEE 37th International Conference on Micro Electro Mechanical Systems (MEMS), 2024.
[39] L. Zhu, K. Wang, T. Ma, L. Huang, B. Xia, S. Zhu, Y. Yang, Z. Liu, X. Quan, K. Luo, D. Kong, J. Huang, Z. Luo, Noncovalent bonding of RGD and YIGSR to an electrospun poly(epsilon-caprolactone) conduit through peptide self-assembly to synergistically promote sciatic nerve regeneration in rats, Adv. Healthcare Mater. 6 (8) (2017), https://doi.org/10.1002/adhm.201600860.
[40] J.K. Sahoo, O. Hasturk, T. Falcucci, D.L. Kaplan, Silk chemistry and biomedical material designs, Nat. Rev. Chem 7 (5) (2023) 302–318, https://doi.org/10.1038/s41570-023-00486-x.
[41] J. Yi, G. Zou, J. Huang, X. Ren, Q. Tian, Q. Yu, P. Wang, Y. Yuan, W. Tang, C. Wang, L. Liang, Z. Cao, Y. Li, M. Yu, Y. Jiang, F. Zhang, X. Yang, W. Li, X. Wang, Y. Luo, X.J. Loh, G. Li, B. Hu, Z. Liu, H. Gao, X. Chen, Water-responsive supercontractile polymer films for bioelectronic interfaces, Nature 624 (7991) (2023) 295–302, https://doi.org/10.1038/s41586-023-06732-y.
[42] T.M. Brushart, P.N. Hoffman, R.M. Royall, B.B. Murinson, C. Witzel, T. Gordon, Electrical stimulation promotes motoneuron regeneration without increasing its speed or conditioning the neuron, J. Neurosci. 22 (15) (2002) 6631–6638, https://doi.org/10.1523/jneurosci.22-15-06631.2002.
[43] A.A. Al-Majed, C.M. Neumann, T.M. Brushart, T. Gordon, Brief electrical stimulation promotes the speed and accuracy of motor axonal regeneration, J. Neurosci. 20 (7) (2000) 2602–2608, https://doi.org/10.1523/jneurosci.20-07-02602.2000.
[44] Z. You, X. Huang, Y. Xiang, J. Dai, L. Xu, J. Jiang, J. Xu, Ablation of NLRP3 inflammasome attenuates muscle atrophy via inhibiting pyroptosis, proteolysis and apoptosis following denervation, Theranostics 13 (1) (2023) 374–390, https://doi.org/10.7150/thno.74831.
[45] S. Shanmughapriya, D. Langford, K. Natarajaseenivasan, Inter and Intracellular mitochondrial trafficking in health and disease, Ageing Res. Rev. 62 (2020) 101128, https://doi.org/10.1016/j.arr.2020.101128.
[46] R. Cartoni, M.W. Norsworthy, F. Bei, C. Wang, S. Li, Y. Zhang, C.V. Gabel, T. L. Schwarz, Z. He, The mammalian-specific protein Armcx1 regulates mitochondrial transport during axon regeneration, Neuron 92 (6) (2016) 1294–1307, https://doi.org/10.1016/j.neuron.2016.10.060.
[47] B. Zhou, P. Yu, M.Y. Lin, T. Sun, Y. Chen, Z.H. Sheng, Facilitation of axon regeneration by enhancing mitochondrial transport and rescuing energy deficits, J. Cell Biol. 214 (1) (2016) 103–119, https://doi.org/10.1083/jcb.201605101.
[48] S.E. Cason, E.L.F. Holzbaur, Selective motor activation in organelle transport along axons, Nat. Rev. Mol. Cell Biol. 23 (11) (2022) 699–714, https://doi.org/10.1038/s41580-022-00491-w.
[49] G. Pekkurnaz, X. Wang, Mitochondrial heterogeneity and homeostasis through the lens of a neuron, Nat. Metab. 4 (7) (2022) 802–812, https://doi.org/10.1038/s42255-022-00594-w.